Self-Organized Mesoscopic Magnetic Structures

Akira Sugawara*, G.G. Hembree and M.R. Scheinfein

Department of Physics and Astronomy, Arizona State University,

PSF-470 Box 871504, Tempe, AZ 85287-1504.

(31 May 1997)

(Revised 26 August 1997)

Abstract

Three types of mesoscopic magnetic microstructure have been formed using self-organization: linear arrays of nanometer diameter islands, nanometer width lines, and undulating, continuous films. These structures were produced by annealing NaCl (110) and (111) surfaces *in situ* to produce patterned templates with 10-100 nm periodicity. Growth parameters such as groove spacing, substrate temperature and total deposit thickness can be varied in order to define specific mesoscopic magnetic structures. The microstructural evolution during growth is discussed in the context of nucleation and coalescence kinetics. The resulting magnetic properties are described, and their connection to the underlying microstructure elucidated.

To be published JAP

PACS numbers: 75.40.Mg, 75.30.Pd, 75.50.Tt

1. Introduction

Mesoscopic magnetic microstructures such as dot and wire arrays are of fundamental interest in the study of coupling and ordering phenomena. From a technological point of view, mesoscopic magnetic structures may produce the future topologies for magnetic storage media. For example, three-dimensional random particle arrays prepared by co-deposition of magnetic and nonmagnetic materials have good high-frequency response and giant magnetoresistance [e.g. 1]. The magnetic properties of these structures depend strongly on the size and spacing of the particles, the concentration of the magnetic element, the growth rate and the substrate temperature [e.g. 2]. Since heterogeneous magnetic particle composites do not have geometrical order, there is no anisotropy in the film plane. However, in-plane anisotropy can be developed by controlling the shape and the spacing of the particles such that the magnetic switching which is characterized by the subtle balance between anisotropy, self-energy, magnetic coupling between particles, and thermal agitation will be well defined.

Specimens with well-defined in-plane anisotropy resulting from specific mesoscopic, geometrical configurations including nanometer size dot and wire arrays have been fabricated by laser-focused atomic deposition [3], electron lithography [4] and local chemical decomposition of metal-organic gas with a scanned probe [5]. Switching mechanisms in these arrays have been studied by magnetic force microscopy [5]. The throughput for producing nanometer size-scale structures with lithographic methods may be low [6], and large areas required for studying macroscopic and collective magnetic properties can be difficult if not impossible to process.

In contrast, our approach is based on self-organization: regular patterns are spontaneously formed in a non-equilibrium system, as in the self-assembling preferential nucleation of hexagonal Co dot arrays on the reconstructed Au(111) surface [7]. We use self-assembly through

shadow deposition on patterned templates, *i.e* the self-masking caused by large-scale surface features. This is a geometrical effect which does not depend strongly on the deposited material. Our method is similar to that proposed by Shinjo [8] who grew a wire array by shadow deposition on a sub-micrometer spaced Si grating that was fabricated by lithography and selective etching. By contrast, we prepare grating templates by self-organization on NaCl non-cleavage ((110) or (111)) planes which become facetted and patterned regularly after thermal annealing [9]. This method allows 10-100 nm spaced, statistically uniform grooves to be formed across centimeter lengths in tens of minutes, though the regularity of the grooves produced by this method is less than that produced lithographically. [10]

We have investigated the relationship between the microstructure and such growth conditions as the annealing temperature of NaCl before deposition, growth temperature and the incident angle of the deposited Fe flux, and the effect on the resultant macroscopic magnetic properties. Three types of the microstructure are described; linear dot arrays, wire arrays, and undulating continuous films. The evolution of the microstructure is explained in terms of nucleation and coalescence kinetics associated with island growth. The magnetization switching processes in these mesostructures which is quite different from those ascribed to flat, continuous Fe films, are also described.

2. Experimental Procedure

Optical-grade (111) and (110) polished NaCl single crystals (miscut angle<3°) were used as substrates [11]. These substrates were etched in deionized water for several seconds to remove surface contamination prior to loading into an ultra-high vacuum growth chamber (base pressure ~ 3×10^{-8} Pa) equipped with Fe electron-beam and SiO thermal evaporation sources. Annealing

these substrates *in situ* produces ordered templates. The annealed (110) oriented substrates form long, straight in-plane macrosteps along [001] as shown in Fig. 1a. The (100) and (010) terraces which result from the thermal annealing process are tilted by 45° with respect to the surface normal. When Fe is deposited at an angle θ with respect to the surface normal $[1\,\bar{1}\,0]$ direction, terraces exposed to the flux nucleate islands which can coalesce and form rectangular wires. When (111) oriented NaCl crystals are annealed, three crystallographically equivalent out-of-plane <100> steps appear as shown in Fig. 1b. Each {100} facet is tilted by 54.7 ° from the template normal. The region exposed to the Fe flux is chevron-hat shaped. The step/chevron separation is determined by the annealing temperature and time. Annealing the NaCl at 350-450°C for 10-15 minutes produces step separations between 10-100 nm. A 10-15 nm SiO passivation layer was deposited directly on both types of stepped NaCl surfaces (normal incidence deposition) since the NaCl substrates must be removed prior to characterization using electron microscopy. The surface topography of the nano-scale stepped NaCl surface is well preserved even after the SiO coating, however, the smooth surface masks the single atomic steps on the NaCl, which might serve preferential nucleation sites. This also prevents the Fe from establishing an epitaxial relationship with the single crystal substrates which is important in island coupling (strength) studies.

Fe was deposited from an electron-beam evaporation source at a rate between 0.03 and 0.20 nm/min. We denote the thickness, *t*, to be that nominal thickness on an exposed terrace in the direction normal to that terrace, e.g. 45 ° off of the (macroscopic) template normal for annealed (110) substrates. The substrate holder could be rotated with respect to the Fe flux direction so that the incident angle of the flux, θ, could be varied from 0° (normal) to 80° (Fig.1). This rotation allowed for a systematic change of the patch (terrace) width exposed to the Fe flux.

The substrate holder could also be translated with respect to the source. A masked substrate was used such that three different thickness films could be grown during a single experiment. After Fe deposition, a 10-15 nm SiO capping layer was deposited to prevent oxidation upon removal from UHV. Thus, the magnetically active Fe layer was embedded in a SiO matrix.

Hysteresis loops were recorded *ex-situ* using the longitudinal magneto-optical Kerr effect (MOKE) [12]. Since both SiO and NaCl are transparent at the He-Ne laser wavelength, and the Fe films were extremely thin, the Kerr intensity was very small. The 2F (first harmonic of the photo-elastic modulator) mode [12] was employed in order to obtain as high a signal-to-noise ratio as possible. Both the sample and the magnet could be rotated with respect to the optical scattering plane to examine the magnetization components parallel and perpendicular to the field, and along and perpendicular to the macrostep (groove) direction.

The microstructure was examined using conventional transmission electron microscopy (TEM: Topcon EM-002B) and high resolution annular dark-field scanning transmission electron microscopy (ADF-STEM: VG HB-501). Specimens were fixed to 200-mesh Cu grids by floating the films off of the NaCl substrates in deionized water. ADF-STEM was required when the Fe particles were smaller than a few nanometers in diameter, and the Z-contrast from the bright field images obtained by TEM was masked by background intensity from the SiO layers. The sizes of individual particles and wires were quantitatively measured using image analysis software.

3. Growth Modes On Facetted Templates

Structures grown on facetted templates include linear arrays of nanometer diameter particles, nanowires with widths of tens of nanometers and lengths of microns or more, and

continuous undulating thin films. The type of structure produced depends upon the structure and length scales present in the NaCl template (L), the incident angle used to deposit the transition metal (θ), and the substrate temperature during growth (T_s). The NaCl (110) surface sublimes and facets to form (100) and (010) terraces during annealing. The depth of the grooves (peak to trough) is ½ the distance between peak tops or groove bottoms (L). The surface area of the facetted surface is always $\sqrt{2}$ times larger than the original (110) surface. Experimentally, we kept the annealing time constant (10 minutes) and altered the annealing temperature, T_a in order to modify the groove spacing (L) between 25 nm (T_a=380°C), 40 nm (T_a=410°C), and 90 nm (T_a=440°C).

The area exposed to the incident Fe flux is determined by geometrical shadowing as depicted in Fig. 1a. The exposed terrace is shadowed by the ridge closer to the evaporation source. Since all terraces are oriented 45° from the surface normal, the percentage of the terrace exposed for a given source angle inclination is constant. However, the distance between exposed areas and the width of each patch can be controlled by modifying the substrate annealing temperature T_a.

Growth temperature is an important parameter used to define microstructure. Fe grows on SiO in a three-dimensional island growth mode. The initial growth is characterized by the competing atomic processes of nucleation, adatom capture and surface diffusion. A detailed numerical analysis of this process has been carried out for the Ag/Ge system [13]. Some of the Fe adatoms diffuse out from the geometrically defined flux region, because an adatom concentration gradient is formed at the mask edge. The nucleation density is expected to be extremely low outside the patch due to low adatom concentration. The grooves can also be preferential nucleation sites. In later stages of growth, coalescence of neighboring islands takes

place. When the growth temperature is high, the round shape of the islands is quickly recovered after two or more neighboring islands touch because surface self-diffusion is fast. This might also cause patch broadening: extending the growth front outward from the defined flux regions. Thus, by varying the separation of the flux-exposed regions through geometrical shadowing, and varying the substrate temperature during growth, different nucleation and growth regimes may be exploited in order to fabricate linear dot arrays, nanowires, and thin, undulating films.

The processes driving the formation of the linear arrays are summarized for high temperature (T_s=190°C) and room temperature growth in Figs.2 and 3 respectively. First, consider the (ideal) growth of a single row of islands along an exposed terrace where the island diameter is approximately equal to the patch width exposed to the deposited Fe flux (Fig. 2a). The growth scheme to form a single particle width-linear array includes the initial nucleation of closely spaced islands (solid outline), adatom capture by existing islands (dotted outline), and finally coalescence (filled). In order to grow this type of array, the initial nucleation density must be in a range where the coalesced particles will be well separated. The diffusion length must be long enough to allow adatoms to incorporate into existing islands, yet short enough to forbid adatoms from diffusing across the ridge or groove to the next terrace exposed to Fe flux. For growth at T_s=190°C, the nucleation density (>2 x 10^{12}cm^{-2}) is maximum where the adatom concentration is maximum (*i.e.* at the patch center in Fig. 2a). When the initial distance between nuclei (< 7 nm) and the initial island diameter (< 2 nm) is smaller than the width of the area exposed to the Fe flux (outlined islands in Fig. 2a), several islands nucleate across the exposed area. During later stages of growth with increased island size, neighboring islands come into contact with each other, but at elevated substrate temperatures, surface diffusion rounds off the Fe island surfaces quickly enough to reduce the surface-energy penalty caused when two

neighboring islands are touching. After each coalescence event, the center of the new island resulting from the coalescence is near the center of the joined islands. Islands join and form 1-dimensional linear arrays through this process. For a specific range of deposited Fe (e.g. t = 1.0 nm or, when exposed areas would have a uniform film thickness of 1.0 nm for the close-packed face of bcc Fe, (110)), the coalesced Fe island diameter (6.7nm) is roughly as wide as the terrace width and the microstructure approaches a 1-dimensional linear particle array. Linear arrays composed of many particles across an exposed terrace can be fabricated by terminating the growth at lower coverages, thereby preventing island coalescence.

During growth at elevated temperatures (T_g=190°C), adatom diffusion is much faster than at room temperature. Elevated temperature growth produces adatom concentration profiles that become broader at the shadow edge. This is schematically depicted in Fig. 2c directly beneath the island profiles in Fig. 2a. At elevated temperatures, a small amount of Fe might escape from the flux-exposed zone due to the adatom concentration gradient formed at the shadow edge, and condense at the groove bottom. Experimentally, this effect appears to be negligible since no islands are observed outside of the area exposed to the Fe flux. This observation indicates that when the thickness is small, most adatoms are captured efficiently by pre-existing islands.

By contrast, linear arrays of nanowires can be fabricated using room temperature growth as illustrated in Fig. 3a. For slow surface diffusion during room temperature growth, the adatom concentration is almost constant in the patch exposed to Fe flux. As a result, a high density of islands uniformly nucleates in the patch (Fig. 3a). The initial islands (diameter < 2nm) are so small that they cannot be clearly resolved by TEM bright-field imaging. Since the profile rapidly drops off at the mask edge (Fig. 3c), the concentration gradient forces a small amount of Fe to escape from the patch and condense at the groove bottom. As such, extremely thin wires are

sometimes observed at the groove bottoms. After the islands (uniformly) cover the patch exposed to the flux, the arriving adatoms are captured by pre-existing (nucleated) islands. The liquid-like coalescence kinetics are slow enough that a network forms (islands fill in) and with increasing coverage, eventually forms a wire, Fig. 3b, whose cross-section when filled in completely is depicted schematically in Fig. 3d. Wire formation is commonly observed over a wide thickness range for room temperature growth. The wire perimeter boundary fluctuates on a size scale determined by the polycrystalline grain size of the individual, coalesced islands. Thus, growth of better wires with sharper edges will require deposition of fine-grained or amorphous materials.

Wire-broadening occurs during high temperature growth (T_g=190°C) which in the extreme case may lead to bridging between adjacent terraces and the formation of continuous undulating films. The wire broadening mechanism at high growth temperatures (T_g>150°C) is summarized in Fig. 2b. With increasing thickness, the wire morphology is completed through a network structure as described above and seen in Fig 2b, however, the faster Fe surface self-diffusion causes the wires to broaden. The amount of Fe escaping from the flux-exposed patch increases causing the ultrasmall wires formed at the bottom of the grooves to be thicker than those formed at room temperature. Broadened Fe patches eventually join the wires at the groove bottom causing the other side of the terrace (not the flux exposed terrace) to be partially covered. At higher coverages, the lines join and form continuous films. Naturally, continuous undulating films can also be trivially fabricated through normal incidence evaporation.

4. Experimental Results

4.1 Linear Dot Arrays

Although the Néel and Brown [14] theories for relaxation in isolated magnetic particles predict relaxation times that are less than microseconds for 6 nm (bulk-anisotropy) diameter Fe particles at room temperature, closely packed mesoscopic linear arrays can be remanent and coercive (ordered), since the long-range fields stabilize moments and extend relaxation times [2]. Such long range interactions have been studied by ferromagnetic resonance [15] , Mössbauer spectroscopy [2,16], mean field calculations and Monte Carlo simulations [17]. Isolating the coupling mechanism is facilitated by the preparation of 3d-transition metal islands in and on insulators like SiO_2 [15], MgO [11] and CaF_2 [17]. This guarantees that the particles do not couple through electronic states in the substrate. Here, we show results on the observed and computed magnetic properties in linear self-assembling arrays of nanometer diameter Fe particles. The formation of linear arrays intrinsically breaks the symmetry in the interaction hamiltonian, thereby stabilizing long range magnetic order.

Fe grows on the SiO base layer in a three-dimensional nucleation and growth mode. During shadow deposition, most Fe islands are localized in the patches exposed to the flux. As shown in Fig. 2, linear dot arrays are formed during the initial stage of high temperature (T_g=190°C) growth on (110) substrates with θ=70°. Fig. 4 shows BF images (first column), ADF images (second column), easy axis (third column) and hard axis (fourth column) MOKE hysteresis loops of the dot arrays grown at 190°C for three different nominal Fe deposition thicknesses: 0.3 nm (first row), 0.6 nm (second row) and 1.0 nm (third row). The spacing of the grooves is 40 ± 12 nm. When θ=70°, 28% of the whole surface is expected to be covered by Fe. The projected patch width is 11 ± 3 nm. Each island is isolated within a patch and no correlation in crystal orientation exists between islands. The island size increases and the density decreases

with increasing total thickness. This behavior is indicative of liquid-like coalescence where a rounded island shape is quickly recovered. Fig. 5 shows the island size distribution obtained from quantitative image analysis of the ADF images. The probability density functions are well fit by a log-normal distribution, as is commonly observed in liquid-like coalescence growth systems [18]. However, the measured geometrical standard deviation obtained here, 1.7, is larger than that observed in normal two-dimensional random particle systems prepared either by evaporation [18] or sputtering [19]. This broadening of the distribution may result from the crossover from a 2-D to a 1-D coalescence system, which is not accounted for in mean-field kinetic coalescence theory [20].

The MOKE loops in Fig.4 show easy-axis behavior when the magnetic field is applied parallel to the arrays, even though each particle is isolated. Experimental MOKE hysteresis loops are shown with solid symbols. Loops were taken along the easy direction, along the wire array (third column), and perpendicular to the wire array, along the hard direction (fourth column). The acquisition time for each loop was on the order of seconds. The computed hysteresis loops from Monte Carlo micromagnetics [10,17] simulations are plotted with solid lines. Immediately evident is the strong asymmetry in the hysteresis loops acquired along and perpendicular to the island-wire direction. The random structure and orientation of the individual particles, the lack of any crystallographic orientation between the particles themselves or between the particles and the substrate, the lack of any interface anisotropy (except in a direction normal to the surface) suggests that the ordering along the island-wire is due to long range interactions through the purely geometric ordering of the island array.

A Monte Carlo micromagnetic model was used to calculate the magnetic properties of the linear arrays as a function of particle radius and density in order to test for dipole-field induced

ordering. One of the main advantages of Monte Carlo is that fluctuations are rigorously included. Simulations used periodic boundary conditions, and between 200 and 400 islands randomly arranged into 3 to 5 wires. The model employs an all-orders interparticle interaction hamiltonian [17]. As input, the model uses the bulk saturation magnetization value, an adjustable externally applied field and the experimentally measured size distribution of Fe islands. The slightly irregular experimental island shapes are approximated by cylinders. Hysteresis loops are calculated by finding an equilibrium magnetization distribution for an externally applied field value. The magnetization accumulators are reset, the external field value changed, and the previous final magnetization state is preserved as the initial distribution for the next Monte Carlo cycle. These computed results indicate that the magnetic moment of each island is influenced by the strong interaction field produced by surrounding particles. The room temperature magnetic phase changes from superparamagnetic to ferromagnetic with increasing particle size [10].

The easy axis hysteresis loop for t=0.6nm film shows an abrupt jump in both the experimental ($H_c < 5$ Oe, our experimental resolution limit) and computed ($H_c < 1$ Oe) loops. The larger islands in the t=1.0nm thick film show easy axis remanence and coercivity in both measured and computed hysteresis loops. Dipole ferromagnetically ordered films have an easy axis along the wire since the shape anisotropy in that direction is small. Since the particles have no preferential crystallographic orientation in the film plane, magnetocrystalline anisotropy is also negligible. Therefore, the anisotropy that orders the array is ascribed to the strong magnetic interaction between self-aligned particles. Since the magnetic-coupling field energy of the islands scales with the island volume, the size dependent remanence is ascribed to temperature stabilization of the magnetization of a particle in the stray field of the surrounding particles.

Another candidate structure for forming ordered ferromagnetic particle arrays uses the

faceting of NaCl (111) as the shadow growth template as illustrated in Fig. 6. Fig.6a and 6b show bright field images of an Fe dot array (t=3nm) formed on a (111) template. The typical patch-to-patch separation is on the order of 100 nm. This distance is geometrically determined by the faceting of the template caused by the thermal etching process, and is independent of nucleation and coalescence kinetics. The equilibrium spacing between islands would normally be $N^{-1/2}$ (where N is the island density) on unfacetted surfaces. Two types of Fe patches, chevron-hat shaped, and parallelogram shaped are observed. The shapes of these two structures can be explained by examining the fluctuations in the peak positions of the etched NaCl(111) surface both in the in- and out-of-plane direction as illustrated in Fig. 6c for the projection shadow mask. The array is neither hexagonal or even regular, and as a result of high temperature growth (T_s=190°C), each chevron patch is composed of several independent islands (Fig.6b). This film did not show strong in-plane magnetic anisotropy as evidenced by the MOKE loop in Fig. 6d, but did have remanence and coercivity. The magnetic interaction between patches is weak due to their large separation, and the shape of the individual patches is not strongly anisotropic on average.

4.2 Wire Arrays

With increasing Fe coverage at room temperature, the space between the islands in the structure shown in Fig. 4 fills in, and wire arrays are formed. Fig. 7 shows bright-field TEM images of wire arrays deposited onto an annealed (110) grating template at room temperature with θ=65°. The Fe wires seen in dark contrast run along the macrosteps of the substrate as shown in Fig. 7a. We confirmed that this microstructure is uniform over the entire 3 mm diameter specimen area of the TEM grid. A corresponding electron diffraction pattern (not

shown here) and a bright field image (Fig. 7b) showed that these wires are polycrystalline Fe with no texture orientation. Therefore, we can neglect the contribution of magnetocrystalline anisotropy to the magnetic properties. The average periodicity of these wires is 90 nm, and their average width (projected) is 30 nm. Both the separation and the width have a broad size distribution due to the inhomogeneous thermal etching during annealing. Furthermore, ultrasmall discontinuous wires (< 10nm in width) intermittently lie at the NaCl groove bottoms between neighboring thick wires. The presence of these ultrasmall wires indicates that a small amount of Fe can escape from the patch and condense at the groove bottom even at room temperature. The aspect ratio of the wires is closely related to the resultant magnetic anisotropy. We estimated the wire length from a foreshortened TEM micrograph (Fig. 7d) that illustrates the long-range imperfection of the wires. The wires are terminated where the terraces perpendicular to the steps (*e.g.* (100)) are accompanied by a miscut from the exact crystal axis. The average wire length calculated from the termination density is about 10μm. Therefore, the aspect ratio is about 200. The demagnetization factor of a magnetic cylinder with this aspect ratio is on the order of 10^{-4}, so strong shape anisotropy is expected. Fig. 7c show easy- and hard-axis MOKE loops for the wire array. Evident is the very strong in-plane anisotropy. The coercivity of the easy-axis loops is typically 2 kOe. Since the diffraction patterns from the arrays indicate that the arrays are indeed polycrystalline, this anisotropy is ascribed to shape anisotropy.

Even though the wire width is determined geometrically by the step spacing and flux inclination angle, arbitrarily small wires could not be obtained on closely-spaced grooves. Figs. 8a and 8b show two different thickness films ((a) t=5nm and (b) t=14nm)grown at room temperature on close-spaced (L=27 nm) grooves produced at T_s=380°C. The grooves are easily filled by a small amount of deposited Fe to form an undulating, continuous film. Even in thin

regions, the fluctuations in the wire width (~ grain size) have the same size scale as the exposed patch width, hence no wires are clearly defined. The magnetic structure of these films is essentially the same as the continuous and undulating films. Figs. 8c and 8d show the same two thickness films as Fig. 8a and 8b grown on a template with wide-spaced (L=87 nm) grooves produced at T_s=440°C. The wire width is similar for both films (different thickness) on the broadly spaced grooves. This width is largely independent of Fe coverage at room temperature, consistent with short diffusion lengths and high nucleation densities discussed above.

In contrast to the wire morphology produced with room temperature growth, wire-broadening was observed for high temperature growth (T_s=190°C). Fig 9a shows a thin film (t=4nm) grown on a wide-spaced (L=87 nm) grating. At this temperature, the transition thickness from a discontinuous to a continuous film increases because compact shapes are quickly recovered after coalescence. Since this thickness is not large enough to form a continuous wire, a network still remains. The width of the patch exposed to the Fe flux is a few times larger than the spacing of the particles, so that one-dimensional linear arrays are not formed. The hysteresis loops for the film in Fig. 9a (adjacent to it) show a coercivity smaller than 1 kOe. Fig. 9b shows a bright field TEM image of 13nm-thick film. At this thickness, the islands grow together, and wires are formed. The wire width is larger than half of ridge-to-ridge distance, and the wire cross-section is asymmetric. This observation suggests that the wire edge diffused outward and joined the thin wires at the groove bottom. The corresponding MOKE loops (adjacent to Fig. 9b) show anisotropic magnetic properties and an easy-axis coercivity larger than 2 kOe.

4.3 Undulating Continuous Films

When Fe is deposited onto the substrate at normal incidence (θ=0°), continuous films having an undulating surface topography are formed. Such undulating films are expected to have different magnetic coupling and domain structure than flat films of the same thickness. Figs. 10a and b show bright field TEM images of such films grown at room temperature and 190 °C respectively along with the corresponding MOKE loops. The films are polycrystalline and continuous, and each grain has an isotropic shape.

The MOKE loops show that the easy-axis is parallel to the macrosteps even though there is no anisotropic grain structure. The coercivities are 400-600 Oe, much larger than that typically found in flat Fe films (smaller than a few tens of Oe). This large coercivity is not due to strain since the large coercivity persists in the film grown at 190 °C, in which the strain is expected to be at least partially relaxed. We examined the magnetization component parallel and perpendicular to the magnetic field by rotating both the magnet and the sample. The results suggested that the switching is done by coherent rotation of the magnetization in the film plane. This behavior is quite different from flat films, in which the switching is caused by domain wall motion. This suggests that the magnetic coupling associated with the surface undulation becomes important. The details of the magnetic switching will be discussed elsewhere.

5.0 Conclusions

Fe was deposited onto annealed NaCl (110) and (111) substrates at various Fe flux incident angles. Three kinds of microstructure, *i.e.* dot array, wire array, and undulating continuous film, were obtained, and they showed strong in-plane magnetic anisotropy. For room temperature growth, Fe condensed in the zone exposed to the flux, such that wire arrays are typically observed. This growth mode is associated with low adatom mobility on the surface. In the high

temperature growth regime, linear dot arrays were observed in the initial growth, because liquid-like coalescence was activated by high adatom mobility.

The nanometer-scale microstructures obtained in this study are statistically uniform over an entire square-centimeter. This type of self-organization can be applied to the fabrication of magnetic devices since the method employs only a simple geometrical shadow effect that does not strongly depend on material combinations. The dot size and separation depends strongly on the growth temperature. Since the nucleation density decreases and coalescence is activated at higher growth temperatures, an array composed of even larger islands is expected to form on large periodicity gratings. Due to NaCl sublimation at high temperatures, the growth temperature cannot exceed 300°C. Similar surface faceting can be expected for materials having anisotropic surface energy. More regular and stable macrostep structures have been found on other materials such as CaF_2 on Si(110) [21], annealed Al_2O_3 [22] and $LiNbO_3$ [23] and Si (311) [24]. These materials are the next candidates for self-organization templates.

Acknowledgments

We are indebted to S. Coyle for technical support and valuable discussions and to Dmitry Streblechencko for providing the custom image processing software. We have also benefited from valuable discussions with K. Schmidt and J. Venables. We would like to acknowledge P. Crozier for taking the ADF images in Fig. 4. This work is supported by the Office of Naval Research under grant No. N00014-93-1-0099. The microscopy was performed at the Center for High Resolution Electron Microscopy at Arizona State University. A. Sugawara is supported by a JSPS postdoctoral fellowship for research abroad.

Figure Captions

Fig.1 Schematic deposition geometry on (a) (110) and (b) (111) templates. The NaCl surface becomes facetted by {100} planes, and long and straight macrosteps run parallel to <100> directions.

Fig.2 Schematic evolution process of wire array at high temperature. Because of high diffusivity of Fe, the initial nucleation density is low and the coalescence kinetics are fast. (a) The initial island nucleation (solid outlined), growth (dashed outlined) and coalescence (solid). (b) At higher coverages, the islands form a continuous network and the wire broadens. (c) Concentration profile across the island array during the initial stages of growth shown in (a). The wire cross section for the structure shown in (b) after more material is deposited. A solid cross-section (asymmetric) is shown.

Fig.3 Schematic evolution process of wire array at room temperature. Because of low diffusivity of Fe, the initial nucleation density is high and the coalescence kinetics are slow. (a) The initial island nucleation (solid outlined), and growth (solid). (b) At higher coverages, the islands form a continuous network. (c) Concentration profile across the island array during the initial stages of growth shown in (a). The wire cross section for the structure shown in (b). The ultrasmall wire seen in the groove sometimes results from adatom escape from the wire and nucleation in the groove.

Fig. 4 Bright-field and annular dark field images and corresponding MOKE loops of one-

dimensional dot arrays grown on a (110) template at 190 °C. Linear array structures become completed with increasing Fe thickness. The MOKE loops show anisotropic behavior even though the particles are not touching. The solid lines are calculated magnetization curves from a Monte Carlo micromagnetics calculation.

Fig.5 Size distribution of islands. The experimental results are well fitted by log-normal distribution (solid lines). Median(μ) and geometrical standard deviation (σ) is summarized in a table (inset).

Fig.6 Dot array formed on a (111) template. (a) Low-magnification TEM image showing both chevron-hat and rectangular shaped patchs. (b) High-magnification TEM image of individual dots. (c) Disordered steps of two types can be observed. (d) MOKE loop.

Fig.7 Typical wire structure of Fe (t = 13nm) and corresponding MOKE loops. (a) Low-magnification BF image showing that the wire array is uniform over large area. (b) High-magnification BF image showing where the ultrathin wire is formed at the bottom of the grooves. (c) Easy- (left) and hard-axis (right) MOKE loops. (d) Foreshortened BF image illustrating how the wires form a network structure on a large scale..

Fig.8 Microstructure formed on grooves of different spacings at room temperature. In Fe films of nominal thickness (a) t = 5nm and (b) t = 14nm grown on narrowly-spaced (L = 27 nm) templates, the grooves are filled quickly by small amounts of Fe. The wire morphology remains constant during growth when the Fe thickness is between (c) t = 5nm and (d) t = 14nm for films

grown on a widely spaced templates, L = 87nm.

Fig.9 Wire structure grown on widely-spaced (L = 87nm) grooves at elevated temperatures (T_s = 190°C). (a) The network structure observed in Fe (t = 4nm) film. The corresponding coercivity is smaller than in the case of a continuous wire array. (b) A broadened continuous wire array (t = 13nm). The wire edges expand past the groove edges, and reach the next facets. The TEM contrast suggests that the wire cross-section is asymmetric.

Fig.10 BF images of undulating continuous films (t = 9nm) grown at (a) T_s = room temperature and (b) T_s = 190°C. The Kerr loops show easy-axis behavior when the field is applied parallel to the grooves, though the in-plane projected microstructures are isotropic.

References

*Present address: Schools of Materials Science, Japan Advanced Institute of Science and Technology, Asahi-dai 1-1, Tatsunokuchi, Ishikawa 923-12, Japan.

[1] J.Q. Xiao, J.S. Jiang, C.L. Chien, *Phys. Rev. Lett.* **68**(25), 3749 (1992); A.E. Berkowitz, J.R. Mitchell, M.J. Carey, A.P. Young, S. Zhang, F.E. Spada, F.T. Parker, A. Hutten, G. Thomas, *Phys. Rev. Lett.* **68**(25), 3745 (1992); A.E. Berkowitz, J.R. Mitchell, M.J. Carey, A.P. Young, D. Rao, A. Starr, S. Zhang, F.E. Spada, F.T. Parker, A. Hutten, G. Thomas, *J. Appl. Phys.* **73**(10), 5320 (1993); M. El-Hilo, K. O'Grady, *J. Appl. Phys.* **76**(10), 6811 (1994).

[2] S. Mörup, *Phys. Rev. Lett.* 72(20), 3278 (1994); S. Mörup, G. Christiansen, *J. Appl. Phys.* 73(10), 6955 (1993); S. Mörup, *Hyperfine Int.* **60**, 959 (1990); S. Mörup, P.H. Christensen, B.S. Clausen, *J. Mag. Mag. Mat.* **68**, 160 (1987); S. Mörup, M.B. Madsen, J. Franck, J. Villadsen, C.J.W. Koch, *J. Mag. Mag. Mat.* **40**, 163 (1983); W-N. Wang, Z-S. Jiang and Y-W. Du, *J. Appl. Phys.*, **78**, 6679 (1995); S. Matsuo, T. Matsuura, I. Nishida and N. Tanaka, *Jpn. J. Appl. Phys.*, 33, 3907 (1994).

[3] R.J. Celotta, R. Gupta, R.E. Scholten and J.J. McClelland, *J. Appl. Phys.*, **79**, 6079 (1996).

[4] J.F. Smyth, S.Schultz, D.R. Fredkin, D.P. Kern, S.A. Rishton, H.Schmid, M.Cali, and T.R. Koehler, *J. Appl. Phys.*, **69**, 5262 (1991), A.O. Adeyeye, G. Lauhoff, J.A.C. Bland, C. Daboo, D.G. Hasko, H. Ahmed, *Appl. Phys. Lett.* **70**(8), 1046 (1997), R.D. Gomez, M.C. Shih, R.M.H. New, R.F. Pease and R.L. White, *J. Appl. Phys*, **80**, 342 (1996); S.Y. Chou, P.R. Krauss and L. Kong, *J. Appl. Phys*, **79**, 6101 (1996).

[5] S S.Gidar, J.Shi, P.F. Hopkins, K.L. Campman, A.C.Gossard, D.D. Awschalom, A.D. Kent, and S. von Molnàr, *Appl. Phys. Lett.*, **69**, 3269 (1996).

[6] A. Fernandez, IEEE-MAG **32**, 4472 (1996).

[7] H. Takeshita, Y. Suzuki, H. Akinaga, W. Mizutani, K. Tanaka, T. Katayama, and A. Itoh, *Appl. Phys. Lett.* **68**, 3040 (1996).

[8] T. Shinjo and T.Ono, *J. Magn. Magn. Meter*, **156**, 11 (1996).

[9] A. Sugawara, Y. Haga and O. Nittono, *J. Magn. Magn. Meter.*, **156**, 151 (1996).

[10] A. Sugawara, S.T. Coyle, G.G. Hembree and M.R.Scheinfein, *Appl. Phys. Lett.*, **70**, 1043 (1997); A. Sugawara and M.R. Scheinfein, *Phys. Rev. Lett.*(submitted).

[11] The NaCl samples were purchased from Bicron, Inc.

[12] Z.J. Yang, M.R. Scheinfein, *J. Appl. Phys.* 74(11) 6810 (1993).

[13] J.A. Venables, F.L. Metcalfe, and A. Sugawara, *Surf. Sci.*, **371,** 420 (1997).

[14] L. Néel, *Ann. Geophys.*, **5**, 99 (1949);A. Aharoni, *Introduction To The Theory Of Ferromagnetism* (Oxford Science Publications, Oxford, 1996).

[15] W-N. Wang, Z-S. Jiang and Y-W. Du, J. Appl. Phys., **78**, 6679 (1995); S. Matsuo, T. Matsuura, I. Nishida and N. Tanaka, Jpn. J. Appl., **33**, 3907 (1994).

[16] S. Linderith, L. Balcells, A. Labarta, J. Tejada, P.V. Hendriksen and S.A. Sethi, J. Magn. Magn. Mater., **124**, 269 (1993).

[17] M.R. Scheinfein, K.E. Schmidt, K.R. Heim, G.G. Hembree , Phys. Rev. Lett, **76**(9), 1541 (1996); K.R. Heim, G.G. Hembree, K.E. Schmidt and M.R. Scheinfein, Appl. Phys. Lett, **67**, 2878 (1995).

[18] C.G. Granqvist and R.A. Buhrman, *J. Appl. Phys.*, **47**, 2200 (1976)

[19] A. Sugawara, Y. Nakamura and O. Nittono. *J. Crys. Growth.*, **99,** 583 (1990).

[20] *e.g.* D. Kashchiev, *Surf. Sci.*, **86**, 14 (1979).

[21] L. Schowalter and R.W. Fathauer, *CRC Critical Review on Solid State and Materials Science*, **15**, 367 (1989).

[22] J. R. Heffelfinger, M.W. Bench and C.B. Carter, *Surf. Sci.*, **343**, L1161 (1995).

[23] W-N. Wang, Z-S. Jiang and Y-W. Du, *J. Appl. Phys.*,**78**, 6679 (1995).

[24] S. Song, M. Yoon, S.G.J. Mochrie, G.B. Stephenson, S.T. Milner, Surf. Sci., **372**, 37 (1997).

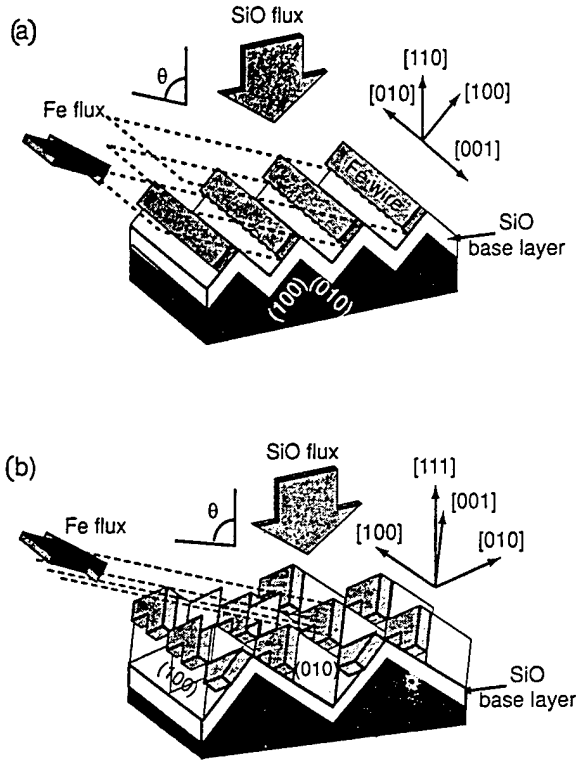

Fig 1
Sugawara

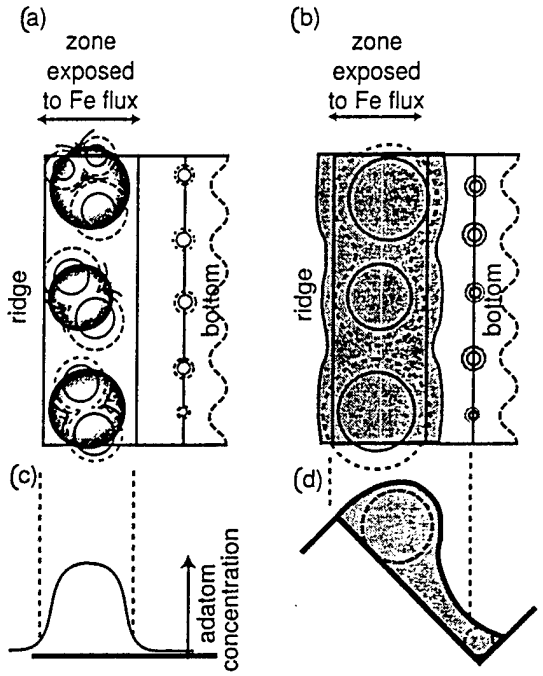

Fig 2
Sugawara

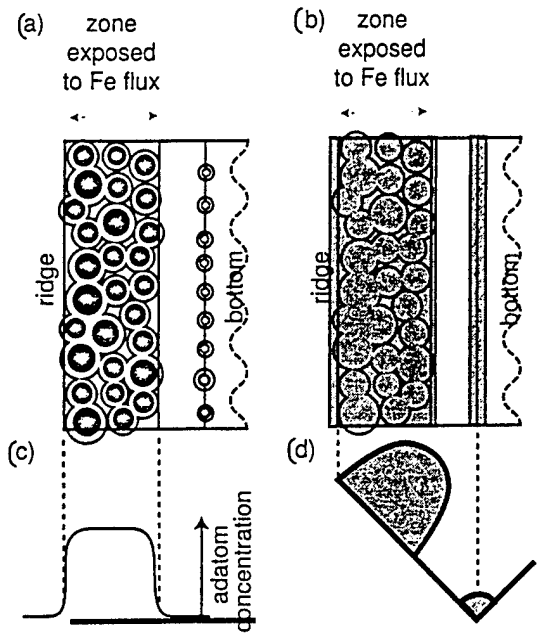

Fig 3
Suzuwara

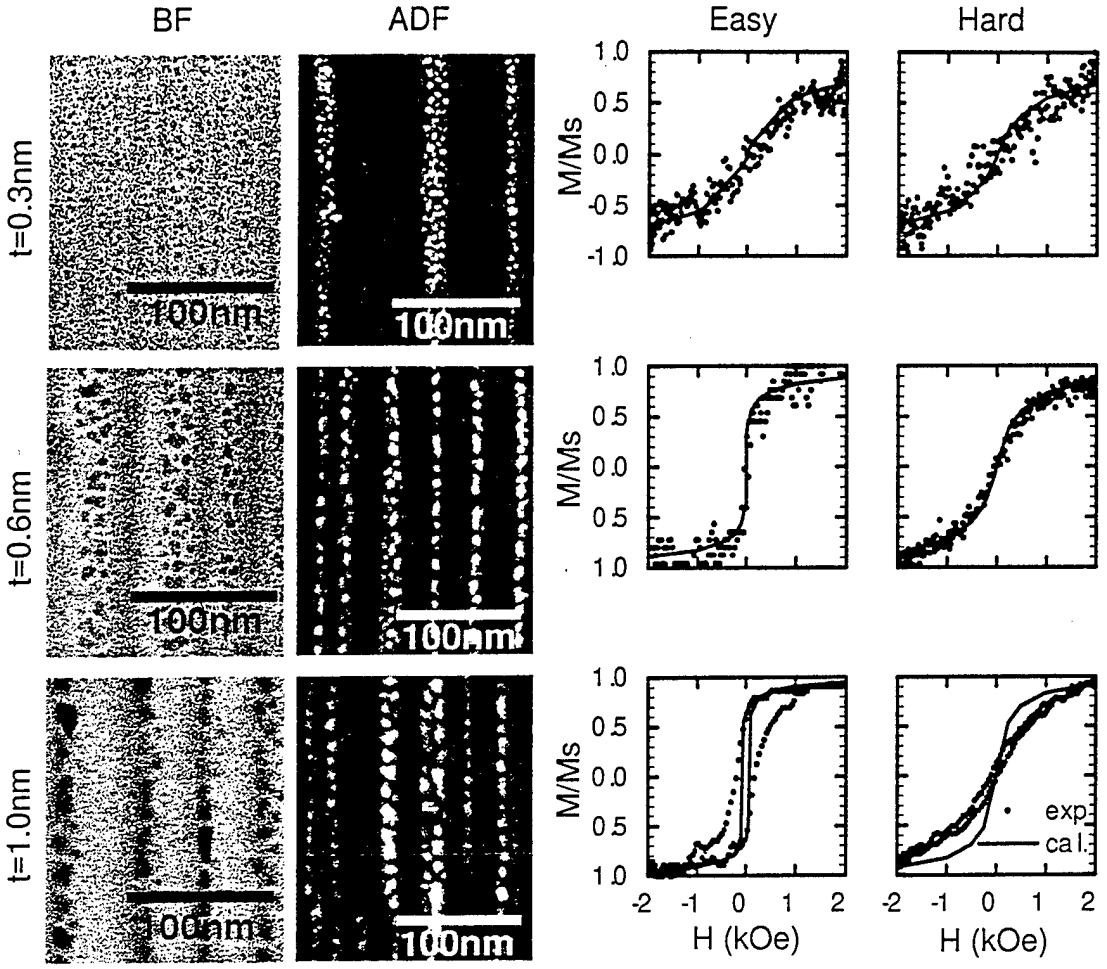
BF
ADF
Easy
Hard
t=0.3nm
t=0.6nm
t=1.0nm
100nm
M/Ms
1.0
0.5
0.0
-0.5
-1.0
exp
cal.
-2
-1
0
1
2
H (kOe)

Fig 4.

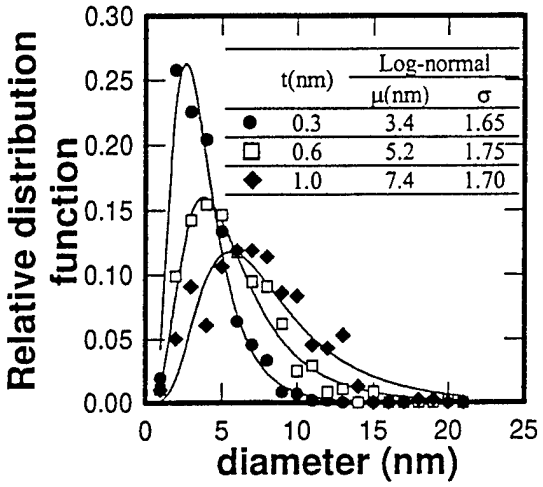
Relative distribution function
0.30
0.25
0.20
0.15
0.10
0.05
0.00
0
5
10
15
20
25
diameter (nm)
t(nm)
Log-normal
μ(nm)
σ
0.3
3.4
1.65
0.6
5.2
1.75
1.0
7.4
1.70

Fig 5

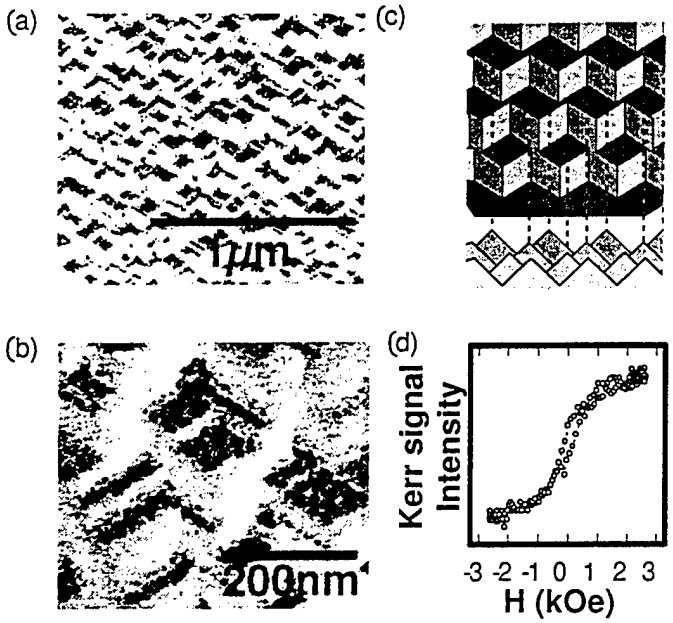

Fig 6
Sugawara

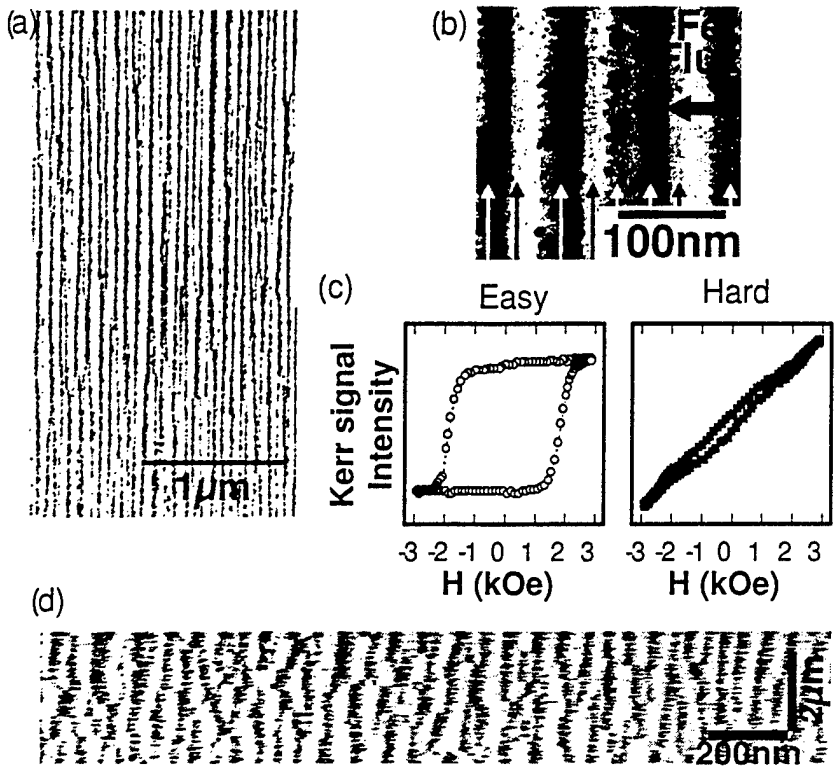

Fig 7
Suzuwara

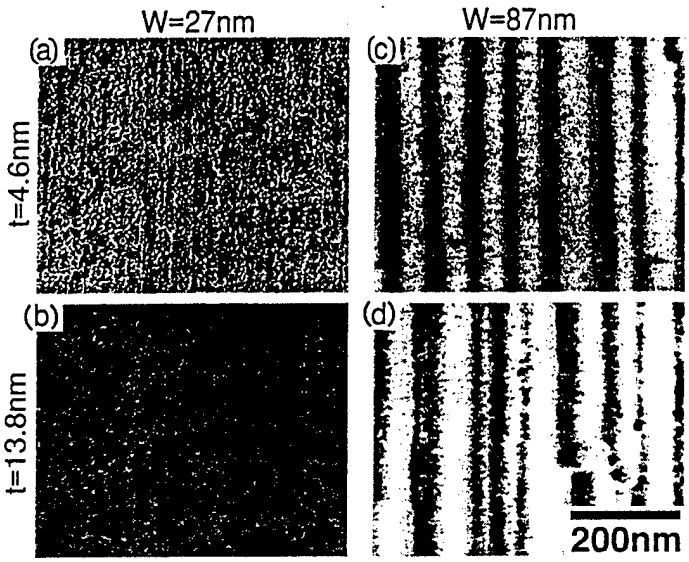

Fig 8
Sugawara

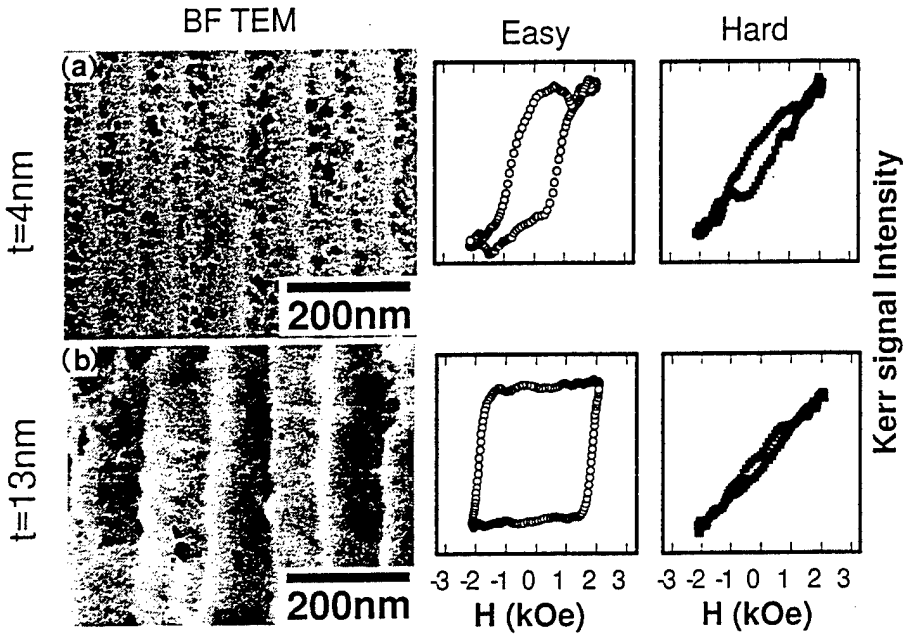

Fig 9
Sugawara
final

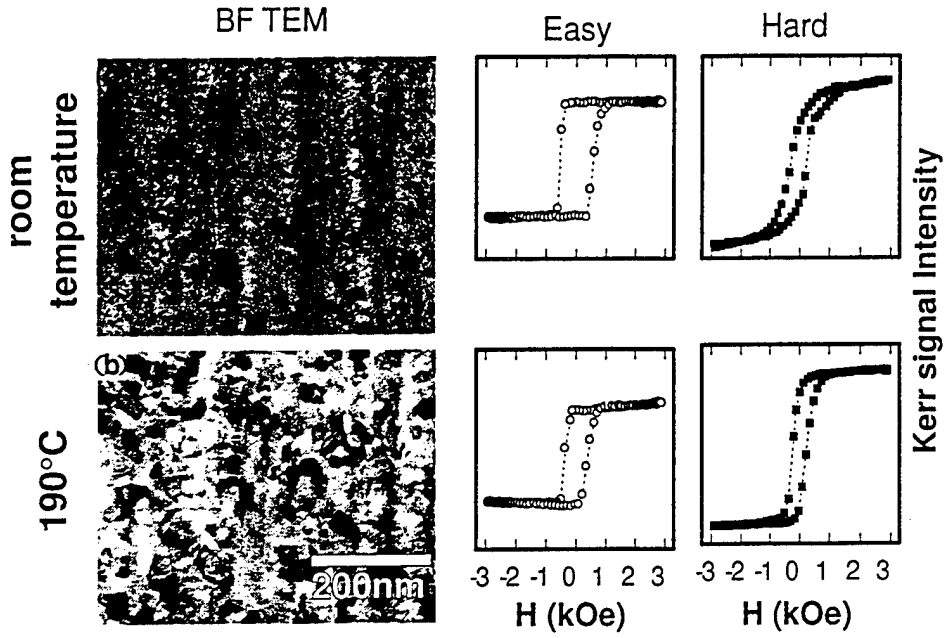

Fig 10
Suzuwaka
(1994)